

GHASP: an $H\alpha$ kinematic survey of spiral and irregular galaxies – IX. The NIR, stellar and baryonic Tully-Fisher relations.*

S. Torres-Flores^{1,2,3†}, B. Epinat^{1,4}, P. Amram¹, H. Plana^{1,5}, C. Mendes de Oliveira²

¹*Laboratoire d'Astrophysique de Marseille, Université de Provence & CNRS,
38 rue F. Joliot-Curie, 13388 Marseille, Cedex 13, France*

²*Departamento de Astronomia, Instituto de Astronomia, Geofísica e Ciências Atmosféricas da USP,
Rua do Matão 1226, Cidade Universitária, 05508-090, São Paulo, Brazil*

³*Departamento de Física, Universidad de La Serena, Av. Cisternas 1200 Norte, La Serena, Chile*

⁴*Institut de Recherche en Astrophysique et Planétologie, Université de Toulouse & CNRS,
14 avenue Edouard Belin, 31400 Toulouse, France*

⁵*Laboratório de Astrofísica Teórica e Observacional, Universidade Estadual de Santa Cruz, Ilhéus, Brazil*

ABSTRACT

We studied, for the first time, the near infrared, stellar and baryonic Tully-Fisher relations for a sample of field galaxies taken from an homogeneous Fabry-Perot sample of galaxies (the GHASP survey). The main advantage of GHASP over other samples is that maximum rotational velocities were estimated from 2D velocity fields, avoiding assumptions about the inclination and position angle of the galaxies. By combining these data with 2MASS photometry, optical colors, $H\alpha$ masses and different mass-to-light ratio estimators, we found a slope of 4.48 ± 0.38 and 3.64 ± 0.28 for the stellar and baryonic Tully-Fisher relation, respectively. We found that these values do not change significantly when different mass-to-light ratios recipes were used. We also point out, for the first time, that rising rotation curves as well as asymmetric rotation curves show a larger dispersion in the Tully-Fisher relation than flat ones or than symmetric ones. Using the baryonic mass and the optical radius of galaxies, we found that the surface baryonic mass density is almost constant for all the galaxies of this sample. In this study we also emphasize the presence of a break in the NIR Tully-Fisher relation at $M_{H,K} \sim -20$ and we confirm that late-type galaxies present higher total-to-baryonic mass ratios than early-type spirals, suggesting that supernova feedback is actually an important issue in late-type spirals. Due to the well defined sample selection criteria and the homogeneity of the data analysis, the Tully-Fisher relation for GHASP galaxies can be used as a reference for the study of this relation in other environments and at higher redshifts.

Key words: galaxies: evolution – galaxies: kinematics and dynamics

1 INTRODUCTION

The Tully-Fisher relation (Tully & Fisher, 1977) is a direct indication of a close relationship between the detected baryons and the total mass in spiral galaxies. The detected baryons consist of the stellar and gaseous content, i.e. the visible mass, and this sets the luminosity profile of the galaxy while the total gravitational mass, which includes the dark matter content (and possibly a component of baryonic dark

matter), sets its rotation velocity. Numerous studies have been carried out to investigate this relation, crucial in determining extragalactic distances (e. g. Pierce & Tully 1988, Tully & Pierce 2000), in the study of evolution of galaxies (e.g. Puech et al. 2008) and also in giving constraints on cosmological galaxy formation models (e. g. Portinari & Sommer-Larsen 2007).

The Tully-Fisher relation is undoubtedly a crucial test for galaxy evolution models and although it has been the focus of a number of studies, its origin is still being debated. A few authors argue a cosmological origin (e. g. Avila-Reese, Firmani & Hernández 1998) while others suggest that this

* GHASP Fabry-Perot data are available at <http://fabryperot.oamp.fr>

† Current address. E-mail: storres@dfuls.cl

relation is regulated by star forming processes (e. g. Silk 1997). On the other hand, the Tully-Fisher relation is related to the stellar populations of galaxies as it is suggested by its steeper slope when the luminosity is measured in the near infrared (NIR) bands, when compared to the slope measured in the optical (e.g. Tully & Pierce, 2000). The use of NIR bands in the Tully-Fisher relation has shown to be extremely useful, because NIR bands present lower internal extinction than optical bands (Verheijen 2001) and the mass-to-light ratio is less contaminated by younger stellar populations, giving a better reflection of the stellar mass of the galaxies.

Luminosities can be converted into stellar masses by scaling them by a given mass-to-light ratio. Thus, instead of linking rotation velocities to luminosities, a few authors have chosen to show the correlation of rotation velocities to stellar masses. This relation is called stellar Tully-Fisher relation (e.g. Bell & de Jong 2001). In order to estimate the whole baryonic mass, the gaseous component should be added to the stellar mass. The relation between luminosities and baryonic masses is called the baryonic Tully-Fisher relation. This relation has been studied by several authors (e. g. McGaugh 2000, Verheijen 2001, Geha et al. 2006, Bell & de Jong 2001). The slope of the baryonic TF relation is an important test for galaxy formation models. A steeper slope indicates that the baryonic mass of massive galaxies tends to approximately match the total mass of the galaxy.

To date, most of the works devoted to study the Tully-Fisher relation have used compilations of several galaxy surveys, observed in different ways (HI line profiles and rotation curves) adding factors of uncertainties due to sample non-homogeneity. Beside the problems of using different samples, the use of certain observational techniques may add other uncertainties in the study of the Tully-Fisher relation. For example, an over or under prediction of the position angle in long-slit observation could produce an erroneous estimate of the maximum velocity of a galaxy, which will be reflected in the Tully-Fisher relation.

In order to avoid the problems listed in the previous paragraph, we have made use of the homogeneous galaxy survey Gassendi H α survey of SPirals (GHASP) to study the NIR, stellar and baryonic Tully-Fisher relations and their implications for the total mass of galaxies. The GHASP survey represents a large effort to constitute a sample of field galaxies in an homogeneous way. First, a strict isolation criterion has been used to insure the isolation of the galaxies. Rather close galaxies have been chosen in order to guarantee a high spatial resolution, compared to HI surveys. High and low inclination objects have been excluded in order to minimize uncertainties in the de-projected rotation curve. Second, all GHASP galaxies have been observed using the same instrument; a scanning Fabry-Perot attached to a focal reducer at the 193 cm at Observatoire de Haute Provence (OHP). In addition to obtaining data for the whole sample with the same instrument, which is a great advantage to insure homogeneity, the scanning Fabry-Perot is certainly the most adapted instrument to obtain rotation curves in the most proper way. Because it gives a 2D velocity field, we can obtain the rotation curve (and the maximum velocity) without any previous assumptions about the position angle or the inclination like it is the case for long-slit observations. This technique avoids, in this way, a great factor of uncertainty that is common to not be taken into account using

other techniques. Third, the data reduction has been performed in an homogeneous way, in order to derive the rotation curves from the velocity fields in the cleanest and most rigorous possible way (see Epinat et al. 2008a,b for details). These three points allowed eliminating (or at least greatly minimizing) several problems that previous studies have encountered. Using rotation curves to obtain the maximum rotation velocity is a more precise way compared to the HI line width profile technique, used by several others studies. The higher spatial resolution of optical velocity maps, compared to HI, avoids the problem of missing the maximum velocity because of lack of resolution (beam smearing).

Together with the kinematic information, we have used H and K-band photometry from 2MASS survey, mass-to-light ratios derived from stellar population models, HI fluxes and H₂ masses from the literature to perform, for the first time, the NIR, stellar and baryonic Tully-Fisher relations for the GHASP sample.

In §2 we describe the data, including the method used to compute the stellar, gaseous and baryonic masses. In §3, we present the results. In §4 we discuss and compare our results with previous works. Finally, we summarize our main findings in §5.

2 DATA

2.1 Rotational velocities

GHASP is the largest sample of spiral and irregular galaxies observed to date using Fabry-Perot techniques. It consists of 3D H α data cubes for 203 galaxies, covering a large range in morphological types and absolute magnitudes. All the GHASP galaxies have been recently reanalyzed in a homogeneous way in Epinat et al. (2008a,b). These authors published velocity fields, monochromatic H α images, dispersion velocity maps, rotation curves and maximum rotation velocities (V_{max}) for each galaxy.

A sub-sample of 93 galaxies has been selected by removing from the sample: 1) galaxies with radial systemic velocities lower than 3000 km s⁻¹ (to avoid the effect of the Local Group infall) for which no other individual measurements of distances were available (the references are indicated in Epinat et al. 2008b) and 2) galaxies with inclinations lower than 25 degrees for which the uncertainties on the rotational velocity is comparatively high.

Rotation curves shown in Epinat et al. (2008a,b) present a large variety of shapes (from falling to rising) and degrees of asymmetry. In order to study the influence of the shape of the rotation curves in the Tully-Fisher relation, we have made a classification of our sample in three subsamples, i. e. rising, flat and decreasing rotation curves, which will be described with the letters “R”, “F” and “D”, respectively. An “+” or “-” sign has been added if the rotation curve is respectively more or less extended than the optical radius of the galaxy (R_{25}). No symbol is added if the radius of the observed rotation curve is barely equal to R_{25} .

A decreasing or flat rotation curve displays a clear V_{max} . This is not the case for a rotation curve which rises up to the very last observed radius, for which V_{max} is possibly underestimated. This is even worse if the rising rotation curve does not reach the optical radius. In this case, V_{max}

was computed at R_{25} by extrapolating an \arctan function ($V(r) = V_0 \times (2/\pi) \times \arctan(2r/r_t)$, where r_t is the core radius) to the rotation curves. If observed rotational velocities at $R < R_{25}$ are higher than the modeled value, the observed values have been used. This could be the case if large scale bumps in the inner parts of rotation curves are present. Table A1 (column 8) presents the results of the rotation curve quality assessments.

The main assumption necessary to derive a rotation curve from the observed velocity field is that rotation motions are dominant and non circular motions are not part of a large-scale pattern. Thus, by construction, a rotation curve provides a measurement, for each radius, of the axisymmetric component of the gravitational potential well of the galaxy. By consequence, if the motions in the galaxy disk are purely circular, the receding and the approaching sides of a rotation curve should match and the residual velocity field should not display any structure. Once the parameters of the rotation curves are properly computed by minimizing the velocity dispersion in the residual velocity field (Epinat et al. 2008), the remaining residuals are the signature of non-circular motions in or out the plane of the disk (e.g. bars, oval distortions, spiral arms, local inflows and outflows, warps), including the intrinsic turbulences of the gas. To quantify the effects of these non-circular motions on the Tully-Fisher relations we have computed, for each galaxy, two indicators. The first one is based on the asymmetries between both sides of the rotation curves, it quantifies the mean difference of amplitude between the receding and approaching sides of the rotation curve. For each ring centered on the galaxy center, the weighted (absolute) velocity difference between both sides is computed. The weight is provided by the number of bins in each ring. Each bin is an independent velocity measurement on the velocity field, it may be constituted by ~ 50 pixels for low signal-to-noise region of the galaxy. Depending of the spatial resolution, each ring contains from two to several hundreds bins. Due to the fact that their radius are smaller, the central rings contains a number of pixels lower than the outer ones, their weights is thus smaller. The second indicator is based on the mean velocity dispersion extracted from the residual velocity field. This parameter is quantified by computing the average local velocity dispersion on the whole residual velocity field. To not overestimate the weight of non circular motion in slowly rotating systems with respect to high rotators, both indicators have been normalized by the maximum rotation velocity. We found that both indicators show the same trend on the Tully-Fisher relation, thus we will only illustrate the results using the indicator related to the asymmetries in the rotation curve.

2.2 Photometry

We computed the near-infrared magnitudes using 2MASS data (Skrutskie et al. 2006). 2MASS H and K-band data were available for 83 galaxies of the GHASP sub-sample defined in section §2.1. Absolute magnitudes were obtained using:

$$M_{H,K} = m_{H,K} + (k_{H,K} - A_{H,K}) - 5 \times \log(D) - 25 \quad (1)$$

Distances (D) were taken from Epinat et al. (2008b). They are computed from the systemic velocities (from the

NED database) corrected from Virgo infall and assuming $H_0 = 75 \text{ km s}^{-1} \text{ Mpc}^{-1}$, except when accurate distance measurements were available (references are listed in Epinat et al. 2008b). The magnitudes $m_{H,K}$ have been computed using the flux within the isophote of $20 \text{ mag arcsec}^{-1}$ (where uncertainties were taken from 2MASS). We corrected the magnitude for Galactic extinction using the Schlegel maps (Schlegel et al. 1998). k-corrections ($k_{H,K}$), extinction due to the inclinations ($A_{H,K}$) and seeing were applied using the method given in Masters et al. (2003). Columns 1, 2 and 3 in Table A1 list the name, H and K-band absolute magnitudes for the sample. K-band luminosities were estimated using $L_K = 10^{-0.4(M_K - 3.41)}$, where the K-band absolute Solar magnitude of 3.41 was taken from Allen (1973).

Given the homogeneity of the *Sloan Digital Sky Survey* (SDSS), g and r-band optical magnitudes were extracted from this database. Moreover, most of the mass-to-light ratio recipes use B-V colors as an input parameter. For this reason, we have converted g and r-band data into B and V-band magnitudes by using the recipes given in Lupton (2000). We have extracted the optical size for each galaxy from the SDSS. In this case, we used the parameter isoA (in the r-band), which corresponds to the diameter of the isophote where the disk surface brightness profile drops to $25 \text{ mag arcsec}^{-2}$. These values were converted in radii (in kpc) by using the distance to each galaxy.

In order to compute the mass-to-light ratio for GHASP galaxies, g-r colors were corrected by Galactic extinction using the values given in the SDSS database and then converted into B-V colors. SDSS colors were available for 45 galaxies from which we removed five objects for which their magnitudes and optical radius are obviously incorrect (compared with the optical radius, and magnitudes, given in HyperLeda). For other six galaxies, there were no radius measurement. All the analysis including the radius of the galaxies were thus performed with 34 objects.

B-band luminosities were estimated by using $L_B = 10^{-0.4(M_B - 5.48)}$, where the B-band absolute Solar magnitude of 5.48 was taken from Binney & Merrifield (1998).

2.3 Mass-to-light ratios and stellar masses

The main uncertainty in the study of the stellar and baryonic Tully-Fisher relations states in the stellar mass-to-light disk ratio Υ_* . Two main methods to estimate this parameter are used. Spano et al. (2008) have modeled the stellar mass distribution of rotation curves, by scaling the R-band surface brightness profile to the rotation curve, obtaining an estimation of Υ_* . Bell & de Jong (2001) have used stellar populations synthesis models to predict a relation between the colors of galaxies and their Υ_* . Although both approaches attempt to compute the same physical parameter, several authors have shown that surprisingly there seems to be no clear correlation between the Υ_* obtained from these two methods (e.g. Barnes et al. 2004). Other authors have invoked the modified Newton dynamics (MOND) to obtain the Υ_* and study its implication on the baryonic Tully-Fisher relation (McGaugh 2005). In this work, we have estimated Υ_* and stellar masses using stellar population synthesis models recipes. One of them consists of simply fixing the value of Υ_* . We have compared our results with other works available

in the literature following the stellar populations synthesis models given by Bell & de Jong (2001, B&J), Bell et al. (2003, BE) and Portinari et al. (2004, PO) (equations 2 and 3, 4 and 5 and 6 respectively).

$$M_{\star}^{\text{B\&J}} = 10^{-0.692+0.652(B-V)} L_K \quad (2)$$

$$M_{\star}^{\text{B\&J}} = 10^{-0.994+1.804(B-V)} L_B \quad (3)$$

$$M_{\star}^{\text{BE}} = 10^{-0.206+0.135(B-V)} L_K \quad (4)$$

$$M_{\star}^{\text{BE}} = 10^{-0.942+1.737(B-V)} L_B \quad (5)$$

$$M_{\star}^{\text{PO}} = 10^{0.730[(B-V)-0.600]-0.115} L_K \quad (6)$$

B&J and BE suggested an uncertainty of 0.1 dex in the Υ_{\star} estimation. The adopted uncertainty in Υ_{\star} is larger than the uncertainties of the optical colors. We have adopted the same uncertainty for the PO relation. B&J used a scaled Salpeter initial mass function (IMF). PO used a Salpeter IMF, with masses ranging between 0.1 and 100 M_{\odot} . These models are available for several colors (to estimate Υ_{\star}) and also for the luminosity in several bands (to estimate the stellar mass). We have converted *SDSS* g-r colors into B-V colors to obtain the Υ_{\star} parameter by using the recipes listed above. Stellar masses were calculated using the K-band luminosities. This band is more likely to be reflective of the stellar mass of galaxies. In order to compare stellar masses derived from the K-band luminosities, we have also used the B-band luminosity, despite the fact that this photometric band could be contaminated with the emission of young stars. We removed from this analysis galaxies for which no *SDSS* colors were available in the literature. Therefore, in the stellar and baryonic analysis, we were left with 45 galaxies in total. K-band luminosities were estimated using $L_K = 10^{-0.4(M_K - 3.41)}$ (see section 2.2).

Stellar masses were also estimated using a fixed mass-to-light ratio following McGaugh et al. (2000, *MG*). These authors defined the mass-to-light ratio in the K-band as $\Upsilon_{\star} = 0.8 M_{\odot}/L_{\odot}$. In this case, the stellar mass is simply:

$$M_{\star}^{\text{MG}} = \Upsilon_{\star} L_K \quad (7)$$

It is interesting to note that Gurovich et al. (2010) estimated the Υ_{\star} for a sample of local galaxies by modeling their stellar population histories. These authors did not find differences in the Tully-Fisher relation when the stellar masses were computed by using the modeled Υ_{\star} or when this parameter was fixed to $\Upsilon_{\star}=0.8$ (McGaugh et al. 2000).

2.4 Baryonic masses

The mass of a galaxy is constituted of its content in stars and stellar remnants, gas (neutral, molecular and a negligible component of ionized gas), dust (usually negligible) and dark matter. The baryonic mass is the sum of the stellar and gas contents. The total mass in gas, M_{gas} , is:

$$M_{\text{gas}} = M_{\text{HI}} + M_{\text{He}} + M_{\text{H}_2} + (M_{\text{HII}}) \quad (8)$$

where M_{HI} is the neutral gas, M_{He} is the mass in helium and metals, M_{H_2} is the mass in molecular hydrogen and M_{HII} is the (negligible) mass in ionized hydrogen.

In order to obtain the baryonic mass for the GHASP sample we have calculated the observed HI mass for each

galaxy using the corrected 21-cm line flux taken from HyperLeda (Paturel et al. 2003). Fluxes were converted into mass using the relation:

$$M_{\text{HI}} = 2.356 \times 10^5 F_{\text{HI}} D^2 \quad (9)$$

where D is the distance to the galaxy in Mpc, and F_{HI} is the HI flux in Jy km^{-1} .

To take into account the correction for helium and metals in the gas content (e. g. McGaugh et al. 2000), M_{He} is related to the HI mass through:

$$M_{\text{He}} = 0.4 M_{\text{HI}} \quad (10)$$

The H_2 mass has been computed following the formula given by McGaugh & de Blok (1997), using the morphological type of the galaxies (Young & Kneese, 1989).

$$M_{\text{H}_2} = M_{\text{HI}} (3.7 - 0.8T + 0.043T^2) \quad (11)$$

Nevertheless, to avoid uncertainties linked to our bad knowledge in the H_2 content, the baryonic mass studied in this paper does not include H_2 , except when it is explicitly mentioned. The baryonic mass, M_{bar} , is defined as:

$$M_{\text{bar}} = M_{\star} + M_{\text{gas}} \quad (12)$$

where M_{\star} is the total stellar mass. Uncertainties in the baryonic mass are the results of the quadratic sum of the uncertainties in stellar masses and uncertainties in the HI masses, which were taken from HyperLeda.

We have compared the baryonic mass to the total dynamical mass for each galaxy of our sample. Although almost the whole baryonic mass is approximately within the optical radius, the total dark matter content is not, thus we compute the dynamical total mass only within the optical radius. To estimate the total dynamical mass, we assumed the mass has a spherical distribution, which is likely the case for the dark halo component, as supported by observations (e.g. Ibata et al. 2001) and N-body simulations (e.g. Kazantzidis et al. 2010) by using:

$$M(R) = \alpha R \times V_{\text{max}}^2 / G \quad (13)$$

where α is a parameter depending on the mass profile distribution (equal to one for an uniform distribution). To compute $M(R)$ we have used the r-band optical radius from *SDSS*, as tabulated in the Appendix. In order to obtain an estimation of the dark matter content at the optical radius, we have subtracted the baryonic mass (as estimated in §2.5) from the dynamical total mass within the optical radius.

2.5 Fitting method

Galaxies having the same rotational velocity do not necessarily have the same luminosity (or reciprocally), thus the observed Tully-Fisher relation presents a dispersion which may be produced by intrinsic properties of galaxies. Beside this dispersion, uncertainties in magnitudes/masses and rotational velocities should be taken into account when the slope and zeropoint of this relation are computed (see Hogg et al. 2010 for details about fitting straight lines). Several efforts have been performed to fit straight lines to fundamental relations, taken into account together the uncertainties in both axis and the intrinsic dispersion of the relation (e. g. Tremaine et al. 2002, Weiner et al. 2006). In this paper,

we have followed the prescription given by Tremaine et al. (2002), by adding (in quadrature) a dispersion factor to the uncertainties estimation of the NIR magnitudes, stellar and baryonic masses. The value of the dispersion factor is chosen in order to reach a χ^2 of unity per degree of freedom. To fit the Tully-Fisher relation, we used linear relation of the form:

$$y = \alpha x + \beta \quad (14)$$

where, $y = M_{H,K}$ and $y = \log(M/M_\odot)$, for the NIR and stellar/baryonic Tully-Fisher relation, respectively, and $x = \log(V_{max}/\text{km s}^{-1})$. To obtain the slope and the zerpoint of this relation, we used the task FITEXY (Press et al. 1992).

3 RESULTS

In Table A1 we list the NIR magnitudes and the different rotational velocities that we obtained, from the observations and from the arctan model (see §2.1). Columns 1, 2 and 3 list the name, H and K-band magnitudes. Column 4 shows the observed maximum rotational velocity for each galaxy. Column 5 gives the modeled velocity at R_{25} . Column 6 corresponds to the rotational velocity used in the TF relation. Finally, in column 7 we classify the shape of rotation curves of the GHASP sample as shown in §2.1.

In Table A3 we list the different determinations of mass-to-light ratios (Υ_*) and masses for each galaxy. Columns 1, 2 and 3 indicate respectively the name, the radius of the galaxies (taken from *SDSS*) and the B-V colors (transformed from g-r colors). In columns 4, 5 and 6 we list the mass-to-light ratios calculated from equations 2, 4 and 6, respectively. Values for the stellar masses are shown in columns 7, 8 and 9, following B&J, BE and PO, respectively. In column 10, we list the $M_{HI}+M_{He}$, where M_{HI} is calculated using the observed H I mass for the GHASP sample. Column 11 corresponds to the baryonic masses excluding the H_2 content ($M_*+M_{HI}+M_{He}$), M_* is here calculated following BE given in column 8.

3.1 H and K-band TF relations

In Fig. 1 (upper panels) we plot the Tully-Fisher relations for the H and K-band (left and right panels, respectively). In both panels, flat, decreasing and rising rotation curves are indicated by black dots, green triangles and red stars, respectively. Galaxies having a rising rotation curve show a large dispersion on the Tully-Fisher relation, while most of the flat rotation curves lie on the relation. This may simply reflect the scatter in the determination of V_{max} for rising rotation curves, for which V_{max} may be uncertain. Alternatively, this might indicated that rising rotation curves, that are usually dark matter dominated galaxies, show an intrinsic scatter in the Tully-Fisher relation. In the bottom panel of Fig. 1 we plot the K-band Tully-Fisher relation in which we divided the sample by their asymmetries in the rotation curve. Galaxies displaying the largest non-circular motions (red stars) lie preferentially in the low velocity/luminosity region of the plot and present a larger scatter than galaxies less affected by non circular motion (black dots). The conclusion is that non-circular motions contribute to the scatter in

the NIR Tully-Fisher relation, at least in the low luminosity (and mass) region of the plot.

Inspecting Fig. 1, we observe a break in the Tully-Fisher relation at $M_{H,K} \sim -20$. This effect has already been noted by McGaugh et al. (2000), Gurovich et al. (2004) and Amorín et al. (2009). In order to quantify this break, we have applied a fit (as discusses in §2.5) to all galaxies (black dashed line) and to the galaxies with $M_K < -20$ (red dotted-dashed lines). For the first case, we have derived the followings equations:

$$M_H = (1.97 \pm 1.36) - (10.84 \pm 0.61)[\log(V_{max})] \quad (15)$$

where we use a dispersion factor of 0.75 in the H-band magnitude.

$$M_K = (2.27 \pm 1.39) - (11.07 \pm 0.63)[\log(V_{max})] \quad (16)$$

where we use a dispersion factor of 0.76 in the K-band magnitude.

For galaxies with $M_K < -20$, we have derived:

$$M_H = (-4.29 \pm 1.14) - (8.18 \pm 0.50)[\log(V_{max})] \quad (17)$$

where we use a dispersion factor of 0.47 in the H-band magnitude.

$$M_K = (-4.02 \pm 1.17) - (8.39 \pm 0.52)[\log(V_{max})] \quad (18)$$

where we use a dispersion factor of 0.49 in the K-band magnitude.

In the equations above we have included the one-sigma uncertainties in the slope and zero point. Three galaxies ($\sim 4\%$ of the sample) are 1σ off the Tully-Fisher relation. These galaxies could have slightly too high magnitudes for their rotational velocities or too low rotational velocities for their magnitudes (upper left region in each panel of Fig. 1). In spite of the rotation curves of these objects reach the optical radius R_{25} , two of them have rising rotation curves (red stars in the left panels of Fig. 1). In this sense, we can not exclude that both galaxies could have higher rotational velocities than the observed values, placing both galaxies on the TF relation. On the other hand, one galaxy has a flat rotation curve (black dot in Fig. 1), meaning that this object already reached its maximum rotational velocity. Two possible scenarios could explain the high near-infrared magnitude of this galaxy. AGN activity, that could enhance the near-infrared magnitude of Seyfert 1 galaxies (Riffel et al. 2009) and/or the contribution of TP-AGB stars into the K-band luminosity (Maraston 1998). TP-AGB stars are often not taken into account in the models and they are quite important specially for stellar populations with ages below 1 Gyr. A detailed study of this galaxy is out of the scope of this paper.

Taking into account the dispersions, the slopes of the H and K-band TF relations are similar, being slightly steeper in the K-band. Table 1 summarizes the fit parameters (denoted by α for slopes and β for the zero points) found for the TF relation in H and K-bands. In the same table we list values of α and β found in the literature.

3.2 The stellar TF relation

In order to compare different estimators of the stellar mass available in the literature, we have calculated the slope and zero points of the stellar TF relations of our GHASP sample

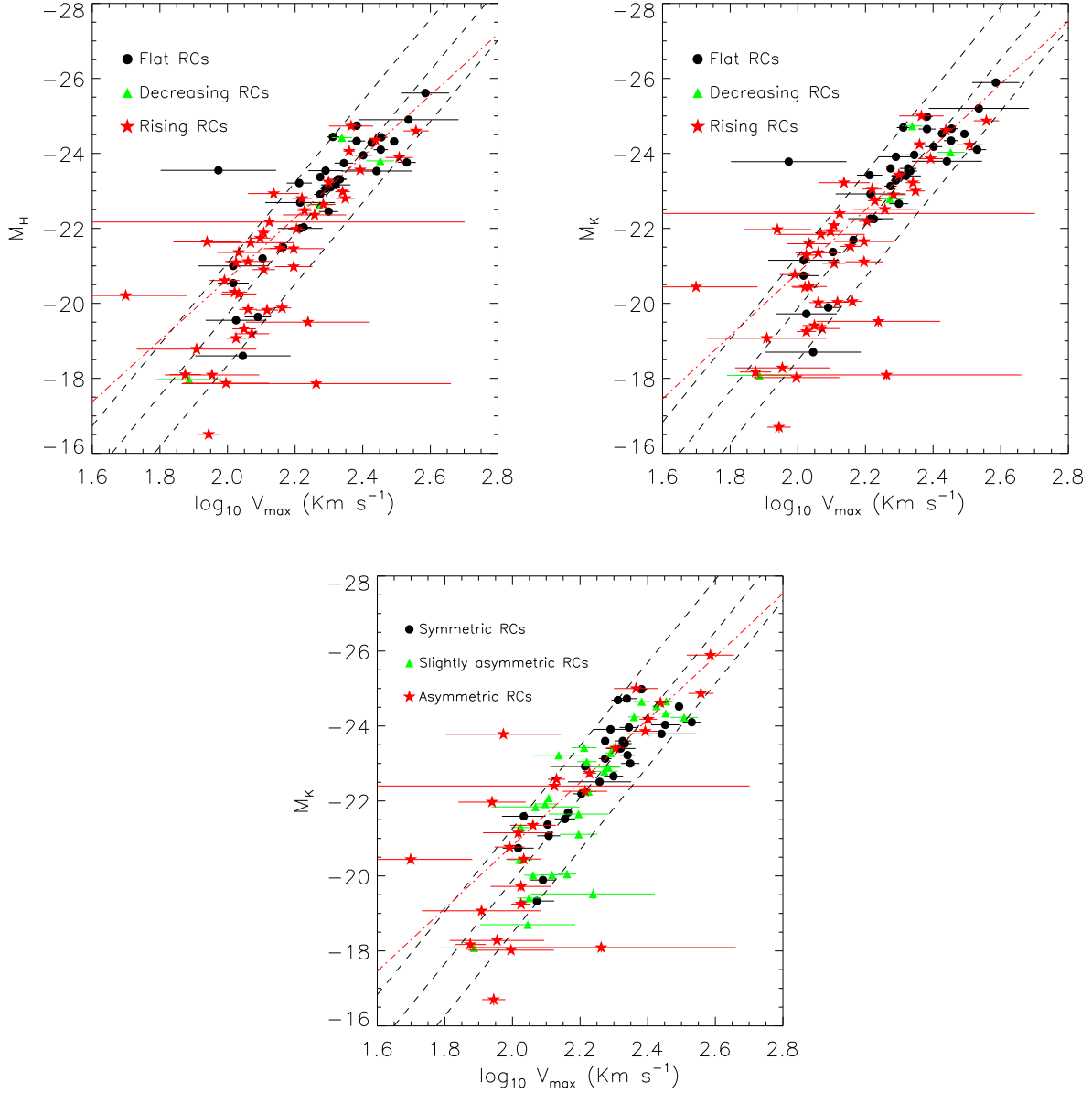


Figure 1. Upper left and right panels: H-band and K-band Tully–Fisher relation for the GHASP sample. The dashed line represents the best fit on all the data (with one- σ in the zeropoint), following $M_{H,K} = (\beta \pm \sigma_\beta) + (\alpha \pm \sigma_\alpha) \log V_{max}$ (see Table 1). The red dashed-dotted line represents the fit for galaxies with $M_K < -20$ (see §3.1). Black dots, green triangles and red stars represent flat, decreasing and rising rotation curves. Bottom panel: K-band Tully–Fisher relation on which galaxies have been distinguished by their ratio between non-circular and circular motions using the asymmetry between both sides of the rotation curve. The sample has been divided in three classes: class I (black dots) is attributed to the galaxies showing the lower non-circular motions; class III (red stars) to the galaxies exhibiting the higher non-circular motions and class II (green triangle) to mild non-circular motions.

using different prescriptions for mass determination given by B&J, BE, PO and MG (see equations 2, 4, 6 and 7). Table 2 summarizes the fit parameters using the different stellar mass estimators. Slopes from different estimators are consistent within 1σ . In the following, we used the BE results to study the stellar and baryonic TF relations (the BE models are updated versions of the B&J models).

In Fig. 2 (left panel), we show the stellar TF relation for the GHASP sample. The central dashed line follows equation 19 (and one- σ in the zeropoint) and represents the best fit

on the data. In this case, we use a dispersion factor of 0.31 dex in the stellar mass.

$$M_\star = 10^{(0.21 \pm 0.83)} V_{max}^{(4.48 \pm 0.38)} \quad (19)$$

We found a slope of 4.48 ± 0.38 (equation 19) when we calculated the stellar masses following BE. B&J found a slope of 4.4 ± 0.2 for the stellar TF relation, for a sample of galaxies in the Ursa Major cluster.

As previously found in the H and K-band TF relation, low-mass galaxies in Fig. 2 (with stellar masses lower than

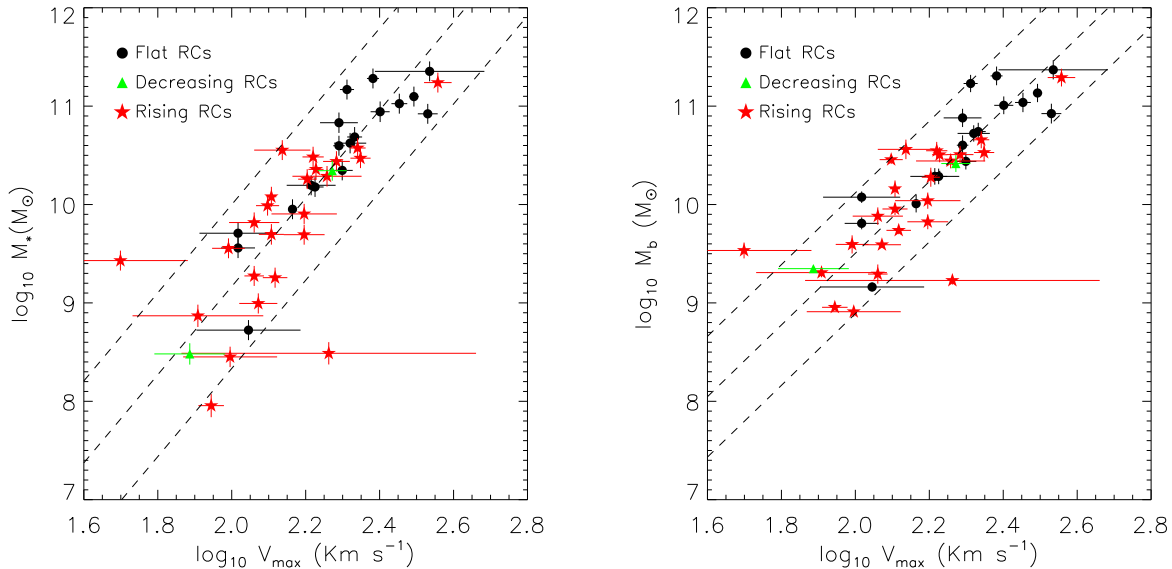


Figure 2. Stellar (left panel) and baryonic (right panel) Tully–Fisher relation for the GHASP sample. The dashed lines represent the best fit on the data (see §2.5). Flat, decreasing and rising rotation curves are represented by circles, triangles and stars, respectively.

$10^9 M_{\odot}$) lie below the relation defined by high-mass spirals. By using cosmological hydrodynamical simulations, de Rossi et al. (2010) suggested that SN feedback is the main responsible for this behavior in low-mass systems.

In Fig. 3 we plot stellar masses derived from the K and B-band luminosities, following the recipes of BE. We found that the B-band luminosities slightly overestimate (underestimate) the stellar mass for the low-mass (high-mass) galaxies, when it is compared with the value derived from the K-band luminosity. Such an overestimation (and underestimation) for the stellar masses of low-mass (and high-mass) galaxies could strongly affect the slope of the baryonic Tully-Fisher relation, adding a “band-dependence effect”. The same trend was found when we use the recipes given in BJ and PO.

3.3 The baryonic TF relation

In Fig. 2 (right panel), we plot the baryonic TF relation for GHASP. The central dashed line represents the best fit for the data and one- σ in the zeropoint (see equation 20). In this case, we use a dispersion factor of 0.21 dex in the baryonic mass. The shapes of the rotation curves are represented by different symbols (circles, triangles and stars indicated flat, decreasing and rising rotation curves).

$$M_{bar} = 10^{(2.21 \pm 0.61)} V_{max}^{(3.64 \pm 0.28)} \quad (20)$$

It is interesting to note that low-mass galaxies now lie on the same relation defined by high-mass galaxies. This fact is attributed to the inclusion of the gaseous mass into the stellar budget. In this plot, the stellar mass was estimated from BE. The slope of the baryonic TF that we derive for the GHASP sample is 3.64 ± 0.28 (which is in agreement with the slope obtained from an unweighted bisector fit, i.e. 3.58 ± 0.37). As done for the stellar mass TF relation, we obtained the slope and zero point of the baryonic TF relation

when the stellar mass was calculated using B&J, BE, PO and MG. These values are listed in Table 3, where α and β correspond to the zero points and slopes, respectively. In Table 3 we have included the resulting slopes and zero points obtained when H_2 masses for the galaxies are included in the baryonic budget. We found that the slope of the baryonic TF relation, when H_2 is included, does not change significantly.

Note, in particular, that the use of the Bell & de Jong (2001) or Bell et al. (2003) mass-to-light recipes, on the GHASP sample, results in a very similar slope of the baryonic TF relation (lines 1 and 9 of Table 3).

In Table 3 we also list the fit parameters for the baryonic Tully-Fisher relation when the stellar masses were derived from the B-band luminosities (and the gaseous mass was corrected by the H_2 gas mass). In this case, the slope is shallower ($\alpha = 3.25 \pm 0.29$) than in the case when stellar masses are computed from the K-band luminosities.

In Fig. 4, we show that, even with some scatter in the relation, the baryonic mass M_{bar} grows almost linearly with the optical galactic radius R_{25} in log units ($M_{bar} = \eta R_{25}^{\gamma}$). We used a weighted bisector least square fit to obtain the dependence between these parameters (we used a bisector fit given that the SDSS database does not quote errors in the radius). We found $M_{bar} = (7.88 \pm 0.01) R_{25}^{(2.39 \pm 0.01)}$, where $\log(\eta) = 7.88 \pm 0.01$. These results suggest that the baryonic mass density, defined by $\Sigma_b = M_{bar}/R_{25}^2$, depends weakly on the sizes of the galaxies. More precisely, $\Sigma_b \propto R_{25}^{0.4}$.

3.4 Total mass versus baryonic mass

In Fig. 5 we have plotted the baryonic mass versus the total mass (computed at the optical radius). This plot shows explicitly the relation between the baryonic and the dark matter content, given that the masses were computed totally independently along the two axis. We fit a least square fit to the data (taken into account errors in both axis), ob-

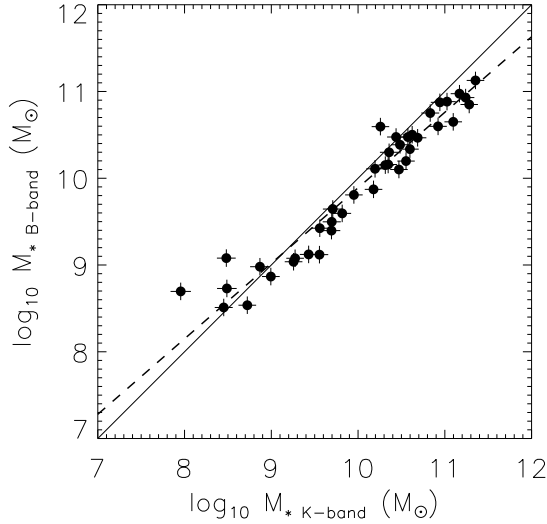


Figure 3. Stellar masses derived by using BE models. In the X-axis masses were calculated using the K-band luminosities while in the Y-axis, stellar masses were calculated using the B-band luminosities. The dashed line represents the best fit on the data and the continuous line represents $y=x$.

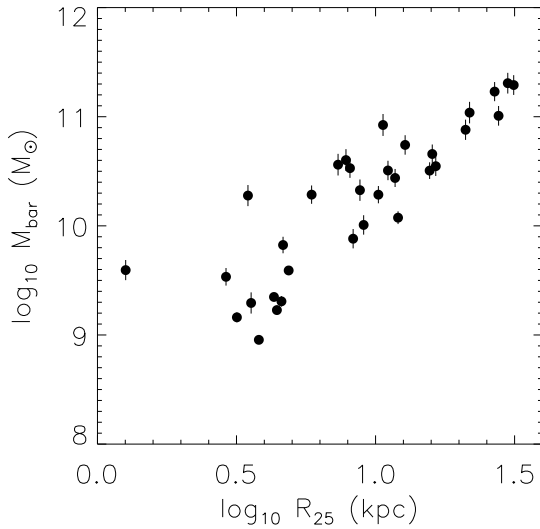


Figure 4. Correlation between R_{25} and the baryonic mass of GHASP galaxies.

taining $M_{bar} = 10^{(-1.51 \pm 0.42)} M_T^{(1.09 \pm 0.04)}$. Given that the slope of this relation is close to one, we have estimated, on average, how much mass we need to add to the baryonic mass to reach the total mass at R_{25} . We have used the ratio $(M_T - M_{bar})/M_T$ at R_{25} (which is an indicator of the dark matter content inside R_{25}) finding a mean value of 0.66 with a standard deviation of 0.17. In this context, we found that, on average, the baryonic mass at R_{25} is about $\sim 34\%$ that of the total mass of the galaxies.

When we divided our sample in low-mass and high-mass

Table 1. H and K-band Tully-Fisher fit parameters

References	H-band	
	α	β
This work	-10.84 ± 0.61	1.97 ± 1.36
Masters et al. (2008)	-9.02	0.06
	K-band	
	α	β
This work	-11.07 ± 0.63	2.27 ± 1.39
Masters et al. (2008)	-10.02	2.37
Courteau et al. (2007)	-9.29	1.24
Karachentsev et al. (2002)	-9.02	...
Verheijen (2001)	-10.60	3.45
Rothberg et al. (2000)	-8.78	-1.22

Comparison between the Tully-Fisher fit parameters (slopes and zero points are represented by α and β , respectively) for this work and other studies available in the literature.

Table 2. Stellar Tully-Fisher fit parameters for the GHASP sample

Model	α	$\log(\beta)$
Bell & de Jong (2001)	4.68 ± 0.40	-0.27 ± 0.88
McGaugh et al. (2000)	4.47 ± 0.54	0.19 ± 1.23
Bell et al. (2003)	4.48 ± 0.38	0.21 ± 0.83
Portinari et al. (2004)	4.70 ± 0.40	-0.11 ± 0.89

Tully-Fisher fit parameters obtained from the ordinary least square bisector fit. Slopes and zero points are represented by α and $\log(\beta)$, respectively.

galaxies, we found that in the first case (GHASP galaxies having rotational velocities lower than 150 km s^{-1}) that 29% of their total mass corresponds to baryonic mass. When we consider intermediate and high-mass galaxies ($V_{max} \geq 150 \text{ km s}^{-1}$), this percentage increase to 37% of the total mass. In general, these results are in agreement with previous works (e.g. Persic et al. 1996).

In Fig. 6 we plot the total-baryonic mass ratio versus the morphological type. Red stars indicated that molecular hydrogen has been taken into account in the baryonic mass estimation and the red dashed-dotted line is its corresponding fit (as described in §2.5 and excluding the outlier with $M_T/M_{bar} \sim 20$). Black dots represent the baryonic mass with no contribution from molecular hydrogen (and the black dashed line represent the fit in this case). From Fig. 6 we can note that the dark halo has a larger contribution to the total mass in late-type spirals (or the contribution of the baryonic mass is less important) than in early-type spirals. When the H_2 is taken into account (red stars), the trend is the same. We found one galaxy (UGC 6628) for which the M_T/M_{bar} ratio was ~ 20 (indicated by an arrow). In this case, the large uncertainty in the maximum rotational velocity (see Table A1) can affect the determination of the total mass, placing this galaxy outside the relation defined by the others galaxies.

We caution the reader that the baryonic matter fractions derived here are dependent on the many assumptions made deriving the color- T_* prescriptions. Most notably,

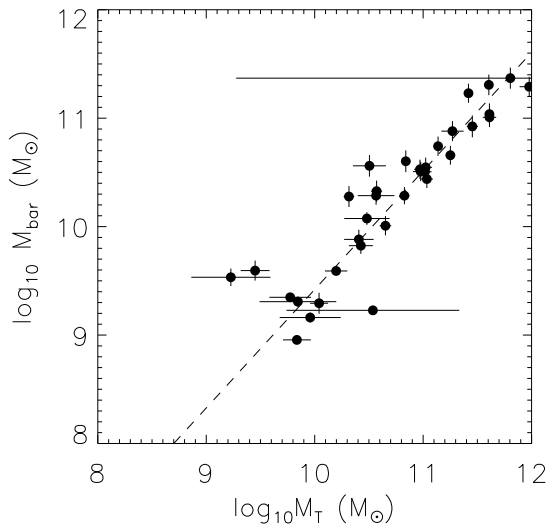


Figure 5. Comparison between dynamical mass at R_{25} and baryonic mass. Dashed line represent a bisector least square fit.

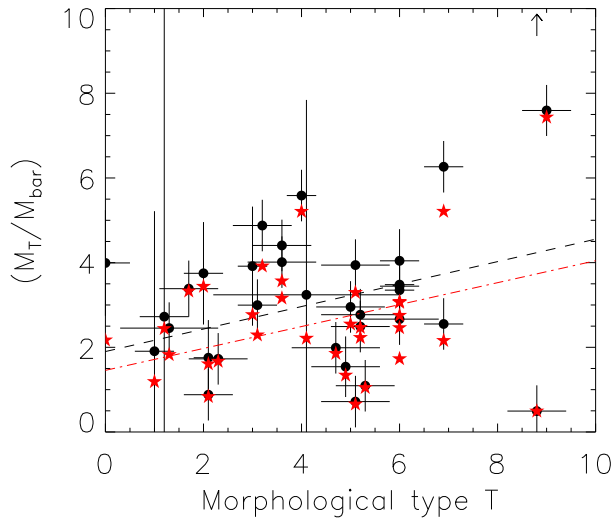


Figure 6. Total-to-baryonic mass ratio versus morphological type. Filled dots represent the gaseous mass used in this work. Stars represent the gaseous mass corrected by H_2 . The least square fit of the filled circles is shown by a dashed lines and the fit of the stars by a dashed-dot-dashed line.

the zero-points of the B&J and BE prescriptions were derived using a maximum disk constraint from rotation curves. Therefore, the baryonic fraction derived here are best seen as upper limits, the baryon fractions could be lower if Υ_* prescriptions were normalized lower.

4 DISCUSSION

4.1 The slope of the baryonic Tully-Fisher relation

In this paper, we have estimated Υ_* for field galaxies using the usual recipes given in B&J, BE and PO. We used these values to compute their stellar and baryonic masses. We found that the slopes of the stellar and baryonic TF relations do not change significantly, whatever the method used for computing the masses. We obtain similar results when we fixed the Υ_* to 0.8 (MG). Table 3 summarizes the different slopes of the baryonic TF relation from different authors using different Υ_* and gas masses. In column 1, this table lists the method used to estimate the Υ_* (BJ01, B03, P04 and MG). Column 2 presents the different samples of galaxies and their references with the resulting slopes and zero points (columns 3 and 4, respectively) using the methods listed in column 1. We computed the results obtained for the GHASP sample for all Υ_* estimators (and also when the H_2 was included in the gaseous mass). We note in columns 5 and 6 which tracer was used for the rotation curve (derived from HI or $H\alpha$ data) and how the gas mass was estimated (HI masses corrected by helium and metals or HI masses corrected by helium and metals and molecular hydrogen).

In the next sections, we compare different slopes of the baryonic TF relation listed in Table 3. Except Kassin et al. (2006), who estimated the maximum rotational velocity from $H\alpha$ data, all the other studies compute the maximum rotational velocity using HI data. In addition to the different models to compute the stellar mass, the main difference between all studies comes from the sample used. B&J used data from cluster galaxies in Ursa Major. Avila-Reese et al. (2008) based their study on a compilation of samples (Zavala et al. 2003) including mostly high surface brightness and late-type disk galaxies complemented with low surface brightness galaxies compiled from the literature. De Rijcke et al. (2007) used dwarf ellipticals galaxies mostly located in groups and clusters and complemented this sample with spirals coming from the study of Tully & Pierce (2000), McGaugh (2005) and Geha et al. (2006). Meyer et al. (2008) used the HIPASS catalog plus 2MASS photometry for a large range of morphological types. Noordermeer et al. (2007) used a sample including massive disk galaxies from the WHISP survey. McGaugh (2005) used a compilation from Sanders & McGaugh (2002), combining late-type galaxies with maximum rotational velocities ranging from 20 to 300 km s^{-1} .

McGaugh (2005) estimated Υ_* , in the B-band, using a maximum disk model, stellar population synthesis models and the mass discrepancy-acceleration relation. Considering these stellar mass-to-light ratios, McGaugh (2005) searched for a slope that minimized the scatter in the baryonic TF relation by using a Υ_* coming from the mass discrepancy-acceleration relation. These authors give a slope of ~ 4 . Using the recipe of Bell et al. (2003) to estimate stellar masses (with a Kroupa IMF), Geha et al. (2006) found a slope of 3.70 ± 0.15 . Using a fixed mass-to-light ratio for a specific band, McGaugh (2005) found a slope of ~ 4 for the baryonic TF relation using galaxies having rotational velocities between $30 \leq V_{rot} \leq 300 \text{ km s}^{-1}$. Stark et al. (2009) and Trachternach et al. (2009) used stellar population synthesis models and obtained a slope of ~ 4 .

Table 3. Fits parameters of the baryonic Tully-Fisher relation

Model	Authors	Coefficients		RC	Gas mass
		α	β		
(1)	(2)	(3)	(4)	(5)	(6)
BJ01	GHASP sample (this work, L_K)	3.72 ± 0.29	2.02	H α	HI+He
	GHASP sample (this work, L_K , H $_2$)	3.69 ± 0.29	2.18	H α	HI+He+H $_2$
	GHASP sample (this work, L_B , H $_2$)	3.27 ± 0.29	3.03	H α	HI+He+H $_2$
	Bell & de Jong (2001)	3.53 ± 0.20	2.73	HI	HI+He
	Avila-Reese et al. (2008) ^a	3.15 ± 0.01	3.59	HI	HI+He+H $_2$
	De Rijcke et al. (2007)	3.15 ± 0.07	3.25	HI	HI+He
	Kassin et al. (2006) ^a	3.40 ± 0.30	2.87	H α	HI+He
B03	Meyer et al. (2008)	4.35 ± 0.14	2.20	HI	HI+He+H $_2$
	GHASP sample (this work, L_K)	3.64 ± 0.28	2.21	H α	HI+He
	GHASP sample (this work, L_K , H $_2$)	3.63 ± 0.28	2.33	H α	HI+He+H $_2$
	GHASP sample (this work, L_B , H $_2$)	3.25 ± 0.29	3.07	H α	HI+He+H $_2$
	McGaugh (2005)	3.19 ± 0.14	3.23	HI	HI+He
	Stark et al. (2009)	3.93 ± 0.07	1.78	HI	HI+He
	Kassin et al. (2006)	3.40 ± 0.30	2.87	HI	HI+He
P04	Avila-Reese et al. (2008)	3.15 ± 0.01	3.59	HI	HI+He+H $_2$
	Geha et al. (2006)	3.70 ± 0.15		HI	HI+He
	GHASP sample (this work, L_K)	3.95 ± 0.31	1.69	H α	HI+He
M00 ^b	GHASP sample (this work, L_K , H $_2$)	3.89 ± 0.30	1.89	H α	HI+He+H $_2$
	Stark et al. (2009)	3.94 ± 0.07	1.79	HI	HI+He
	GHASP sample (this work, L_K)	3.54 ± 0.37	2.44	H α	HI+He
M00 ^b	GHASP sample (this work, L_K , H $_2$)	3.54 ± 0.37	2.52	H α	HI+He+H $_2$
	McGaugh et al. (2000)	3.98 ± 0.12	1.57	HI	HI+He
	Noordermeer & Verheijen (2007)	3.36 ± 0.10	2.14	HI	HI+He
	Pfenniger & Revaz (2005)	3.36 ± 0.10	3.11	HI	HI+He
	Gurovich et al. (2010)	3.20 ± 0.10	2.50	HI	HI+He

Notes. ^a: Stellar mass estimated from B&J and BE. Coefficients follow $M_{bar} = (c \pm \sigma_c) V_{max}^{(\alpha \pm \sigma_\alpha)}$, where $\log(c \pm \sigma_c) = \beta \pm \sigma_\beta$. ^b: In this case we use an unweighted bisector fit (given that we assume a constant Υ_*).

On the other hand, De Rijcke et al. (2007) found a slope of 3.15 ± 0.07 for the baryonic TF relation for a sample of early and late-type galaxies. McGaugh (2005) found a similar slope of $\alpha = 3.19 \pm 0.14$ when he derived stellar masses using stellar population synthesis models of Bell et al. (2003). Fixing the Υ_* to 0.8, Noordermeer & Verheijen (2007) found slopes ranging from 3.04 ± 0.08 to 3.38 ± 0.10 , depending of the adopted rotational velocity. Kassin et al. (2006) found slopes of 3.3 ± 0.3 and 3.1 ± 0.3 , also depending on the adopted rotational velocity.

Using the method given in BE for the stellar mass determination, the GHASP slope of the baryonic Tully-Fisher relation is $\alpha = 3.52 \pm 0.27$. Taking into account the uncertainties, we found that this value is in agreement with most of the results listed above.

As already mentioned in §2.3, there is no consensus in the literature about the correlation that should exist between dynamical and stellar populations synthesis estimations of Υ_* . On one hand, Barnes et al. (2004) did not find a clear trend between the Υ_* and (B-R) color (as predicted by Bell et al. (2003), while de Block et al. (2008) and Williams et al. (2009), found one. These differences could depend on the dynamical mass model used. Barnes et al. (2004) argue that it is difficult to have a reliable estimate of Υ_* without a good knowledge of the dark matter content of galaxies. On

the other hand, Williams et al. (2009) do not use rotation curves in order to derive Υ_* , but a dynamical stellar modeling and compare it with observed rotation curves. Williams et al. (2009) found a median Υ_* of 1.09 in the K-band. If we use the same value to obtain the slope of the baryonic TF relation for the GHASP sample, we found a slope of 3.61 ± 0.37 in good agreement with all the estimations of the slope using stellar population models.

4.2 Baryonic, stellar and total masses in the GHASP sample

The slope of the baryonic TF relation is a test for galaxy formation models, given that they try to reproduce the main properties of observed galaxies (e. g. Portinari et al. 2007). Fig. 5 illustrates that a steeper slope in the baryonic TF relation indicates that high mass galaxies tend to have their baryonic masses better matching their total masses while, in contrast, the fraction of baryonic mass over the total mass decreases for low-mass galaxies. In the case of GHASP galaxies, low-mass galaxies ($V_{max} < 150 \text{ km s}^{-1}$) seem to be dominated by dark matter (corresponding to 71% of their total masses), while intermediate and high-mass spirals ($V_{max} > 150 \text{ km s}^{-1}$) are baryonic matter dominated (corresponding to 37% of their total masses).

Due to the simple model we used to compute the total dynamical masses, these baryonic mass fractions are probably lower limits. Indeed, the total mass within the optical radius is distributed between a spheroidal dark matter halo and a thin optical disk and not simply within a simple spherical distribution. For a given galaxy mass enclosed in a spheroid, the circular speed decreases by $\sim 20\%$ when the axis ratio of the spheroid increases from 0.1 (disk case) to 1.0 (spherical case, Binney & Tremaine 2008, Lequeux 1983). Thus, to take into account the geometry of the system composed of a flat disk and a spherical halo, we have estimated the total dynamical mass should be lowered by a factor depending on the disk-to-halo mass ratio. This increases the fraction of baryonic matter to 31% for low mass galaxies and to 38% for intermediate and high mass systems. Both approaches lead to the same main conclusion: low-mass galaxies have lower baryonic fractions than high-mass galaxies.

The question whether dark matter is coupled with some baryonic mass component of galaxies is still unanswered. Pfenniger, Combes & Martinet (1994) suggest that cold molecular gas could explain the dark matter content in galaxies. Hoekstra et al. (2001) have used a scaling in the neutral hydrogen of galaxies to explain the dark matter in spiral galaxies. In the optical, this analysis is difficult to lead due to the limited extension of optical rotation curves versus HI ones.

In Figs. 4, 5 and 6 we have shown relations between the total and baryonic masses and how these values are related with radius and Υ_* . As expected, we found that larger galaxies exhibit larger amounts of baryonic matter (e. g. Kassin et al. 2006), suggesting that the baryonic mass density (Σ_{bar}) is weakly dependent on the size of the galaxy.

An important issue related to the Tully-Fisher relation is the photometric band used in its construction. B&J found that the stellar and/or baryonic Tully-Fisher relations are independent of the passband used. This result is expected and very important, because we have to consider the total mass of a galaxy in the baryonic mass budget. In our case, we found a difference in the slope of the baryonic Tully-Fisher relation when the stellar mass is calculated from B or K-band luminosities (see Table 3). There are a number of possible causes. One possible explanation could come from the way that luminosities are computed. In the case of the K-band, we have used the total magnitude at the isophote of 20 mag arcsec $^{-2}$, while in the case of the B-band, we have used *SDSS* g-band magnitudes, which were converted into B-band. To check this issue, we also used a Kron elliptical aperture magnitude to estimate the K-band luminosities. Using this alternative method, the slope of the baryonic Tully-Fisher relation is in agreement with the value obtained by using the luminosities at the isophote 20 mag arcsec $^{-2}$ (the difference between both estimations is about ~ 0.05) and therefore the difference with the B-band analysis remains.

Additional reasons why the B and K-band slopes do not agree may be: (1) the extinction corrections between both bands are quite different and may be incorrect; (2) the Υ_* prescriptions of the various groups which differ substantially, especially in the K-band and other near IR passbands (for instance assumptions for star formation histories and metallicity spread may differ) and (3) the stellar population syn-

thesis models that underlie the SED- Υ_* prescriptions show substantial differences in the near-IR, because these passbands are dominated by late stages of stellar evolution that are still poorly understood. Most notably is the importance of TP-AGB stars, discussed in §3.1, but also other evolved stages could play a role.

4.3 Cosmological predictions of the baryonic Tully-Fisher relation

In the past years, several studies have been devoted to study the Tully-Fisher relation using cosmological simulations (e. g. Bullock et al. 2001, Governato et al. 2007, Portinari & Sommer-Larsen 2007 and Piontek & Steinmetz 2009). These authors found slopes shallower than 4 for the baryonic TF relation. For instance, Bullock et al. (2001) found a slope of 3.40 ± 0.05 and Steinmetz & Navarro (1999) suggest a slope of 3 in the standard CDM universe. Portinari & Sommer-Larsen (2007) found an excellent agreement between the predicted baryonic TF relation and the relation obtained by McGaugh (2005) using stellar populations. Our slope $\alpha = 3.64 \pm 0.28$ is in agreement (in one- σ) with the results shown by Bullock et al. (2001). We note that the slope of the baryonic TF for the GHASP sample ($\alpha = 3.64 \pm 0.28$) is steeper than the value expected from the virial theorem: $M_{vir} \propto V_{vir}^3$, however, a steeper slope is expected when the concentration of the halo is taken into account (Bullock et al. 2001).

Several authors have suggested that low-mass galaxies could have higher ratios of dark-to-luminous ratios (Tinsley 1981, Persic, Salucci & Stel 1996, Côté, Carignan, & Freeman 2000). Some of the physical processes associated with that phenomena could be supernova feedback (van den Bosch 2000) and ram pressure stripping of gas (Mori & Burkert 2000). Using morphological types, we have shown that late-type spirals in the GHASP sample have higher total-to-baryonic masses ratio than early-type spirals (even when H_2 gas mass is included in the baryonic mass budget, see Fig. 6). This is in quantitative agreement with most current galaxy formation models under the assumption that the Υ_* prescriptions are applicable and correct over the full mass range of galaxies in the GHASP sample.

5 SUMMARY AND CONCLUSIONS

The main focus of this paper is the study of the NIR, stellar and baryonic Tully-Fisher relation for an homogeneous sample of local galaxies, and determine their implications in the total mass of galaxies. In that frame, we have used the survey GHASP. Given that maximum velocities for GHASP galaxies were derived from rotation curves computed from 2D velocity fields, we were able to minimize the uncertainties. This allows us to determine the maximum rotational velocity of galaxies without any previous assumption about the inclination and position angle of the object. Thus, the GHASP survey is an ideal laboratory to study the Tully-Fisher relation in an homogenous way.

In the following, we list the main findings of this work:

(i) We estimated the slope of the NIR, stellar and baryonic Tully-Fisher relation for the GHASP survey. We have

found a slope of $\alpha = 3.64 \pm 0.28$ for the baryonic Tully-Fisher relation, as estimated by using the BE model. In the case of the baryonic relation, we found that whatever model is used to estimate Υ_* (B&J, BE, PO or MG), the slope of the baryonic Tully-Fisher relation does not change significantly. Recent cold dark matter galaxy formation models are consistent with our results.

(ii) The baryonic mass of a galaxy grows almost linearly with its optical radius. This means that the surface baryonic mass density is weakly dependent on the size of the galaxies ($\Sigma_b \propto R_{25}^{0.4}$).

(iii) We have classified the shape of the rotation curves in order to study their influence on the Tully-Fisher relation. We found that rising rotation curves tend to be farther from the fit than flat rotation curves. We found that galaxies having asymmetric rotation curves, or alternatively galaxies showing larger residual velocities, are also the galaxies presenting the higher dispersion in the Tully-Fisher relation. The fact that only the dispersion of the Tully-Fisher relation (and not the slope or the zeropoint) is affected by the shape and the asymmetries of the rotation curves shows that maximum rotation velocity determinations are rather robust regardless the quality of the rotation curve.

Here we list the results that we have strengthened and clarified by using the GHASP survey:

(i) We bear out the presence of a break in the NIR Tully-Fisher relation at $M_{H,K} \sim -20$ in the sense of low-luminosity galaxies being less luminous (or having higher rotational velocities) than the values expected from the Tully-Fisher relation defined by high-mass galaxies.

(ii) Taken into account the uncertainties, the slope of the baryonic Tully-Fisher relation for the GHASP survey is in agreement with the slope found by Bell & de Jong (2001), Kassin et al. (2006), Geha et al. (2006).

(iii) This work supports that late-type spiral galaxies (which are usually low-mass galaxies) present higher total-to-baryonic mass ratios than early-type spiral galaxies, in agreement with previous observations and with cold dark matter simulations. In this sense, high (low) total-to-baryonic mass ratio may be explained either by a high (low) dark matter content or (and) low (high) baryonic content. Low (high) baryonic content could be explained by the escape of a fraction of the baryons to the intergalactic medium (internal feedback). Alternatively there could be the case that the baryons never collapsed that much into the centers of low mass dark matter halos, i.e., that high mass galaxies have more concentrated baryon distributions than low mass galaxies for this reason.

ACKNOWLEDGMENTS

We would like to thank the anonymous referee for the very useful comments that improved this paper considerably. This publication makes use of data products from the Two Micron All Sky Survey, which is a joint project of the University of Massachusetts and the Infrared Processing and Analysis Center/California Institute of Technology, funded by the National Aeronautics and Space Administration and the National Science Foundation. S. T-F. acknowledges the financial support of FONDECYT through a

post-doctoral position, under contract 3110087 and also to FAPESP (doctoral fellowship, under contract 2007/07973-3). S. T-F also acknowledges the financial support of EGIDE through an Eiffel scholarship and also the AR-CUS program. CMdO acknowledges support from FAPESP (2006/56213-9) and CNPq. HP acknowledges financial support from CNPq (201600/2009-9 and 471254/2008-8). We also acknowledge the usage of the HyperLeda database (<http://leda.univ-lyon1.fr>). S. T-F. and HP would like to thank the staff members of the Laboratoire d'Astrophysique de Marseille for their hospitality when part of this work was developed.

REFERENCES

- Allen, C. W. 1973, *Astrophysical Quantities* (London: The Athlone Press)
- Amorín, R., Aguerri, J. A. L., Muñoz-Tuñón, C., Cairós, L. M. 2009, *A&A*, 501, 75
- Avila-Reese, V., Zavala, J., Firmani, C., Hernández-Toledo, H. M. 2008, *AJ*, 136, 1340
- Barnes, E. I., Sellwood, J. A., Kosowsky, A. 2004, *AJ*, 128, 2724
- Bell, E. F., & de Jong, R. S. 2001, *ApJ*, 550, 212
- Bell, E. F., McIntosh, D. H., Katz, N., & Weinberg, M. D. 2003, *ApJS*, 149, 289
- Binney, J. & Merrifield, M. 1998, *Galactic astronomy* (Princeton Series in Astrophysics)
- Bullock, J. S., Kolatt, T. S., Sigad, Y., Somerville, R. S., Kravtsov, A. V., Klypin, A. A., Primack, J. R., Dekel, A. 2001, *MNRAS*, 321, 559
- Carignan, C., Freeman, K. C. 1985, *ApJ*, 294, 494
- Côté, S., Carignan, C., Freeman, K. C. 2000, *AJ*, 120, 3027
- Courteau, S., Dutton, A. A., van den Bosch, F. C., MacArthur, L. A., Dekel, A., McIntosh, D. H., Dale, D. A. 2007, *ApJ*, 671, 203
- de Blok, W. J. G., Walter, F., Brinks, E., Trachternach, C., Oh, S.-H., Kennicutt, R. C. 2008, *AJ*, 136, 2648
- De Rijcke, S., Zeilinger, W. W., Hau, G. K. T., Prugniel, P., Dejonghe, H. 2007, *ApJ*, 659, 1172
- de Rossi, M. E., Tissera, P. B., Pedrosa, S. E. 2010, *A&A*, 519A, 89
- Epinat, B., Amram, P., Marcelin, M., Balkowski, C., Daigle, O., Hernandez, O., Chemin, L., Carignan, C., Gach, J.-L., Balard, P., 2008, *MNRAS*, 388, 500
- Epinat, B., Amram, P., Marcelin, M. 2008b, *MNRAS*, 390, 466
- Geha, M., Blanton, M. R., Masjedi, M., West, A. A. 2006, *ApJ*, 653, 240
- Governato, F., Willman, B., Mayer, L., Brooks, A., Stinson, G., Valenzuela, O., Wadsley, J., Quinn, T. 2007, *MNRAS*, 374, 1479
- Gurovich, S., Freeman, K., Jerjen, H., Staveley-Smith, L., Puerari, I. 2010, *AJ*, 140, 663
- Gurovich, S., McGaugh, S. S., Freeman, K. C., Jerjen, H., Staveley-Smith, L., De Blok, W. J. G. 2004, *PASA*, 21, 412
- Hoekstra, H., van Albada, T. S., Sancisi, R. 2001, *MNRAS*, 323, 453
- Hogg, D. W., Bovy, J., Lang, D. 2010, *arXiv1008.4686*
- Ibata, R., Lewis, G. F., Irwin, M., Totten, E., & Quinn, T. 2001, *ApJ*, 551, 294
- Kassin, S. A., de Jong, R. S., Weiner, B. J. 2006, *ApJ*, 643, 804
- Kazantzidis, S., Abadi, M. G., Navarro, J. F. 2010, *ApJ*, 720L, 62
- Lequeux, J. 1983, *A&A*, 125, 394
- Lupton 2005, SDSS website
- Maraston, C. 1998, *MNRAS*, 300, 872
- Masters, K. L., Springob, C. M., Huchra, J. P. 2008, *AJ*, 135, 1738

- McGaugh, S. S. 2005, *ApJ*, 632, 859
- McGaugh, S. S., 2004, *ApJ*, 609, 652
- McGaugh, S. S., Schombert, J. M., Bothun, G. D., & de Blok, W. J. G. 2000, *ApJ*, 533, L99
- McGaugh, S. S., de Blok, W. J. G. 1997, *ApJ*, 481, 689
- Meyer, M. J., Zwaan, M. A., Webster, R. L., Schneider, S., Staveley-Smith, L. 2008, *MNRAS*, 391, 1712
- Mori, M., Burkert, A. 2000, *ApJ*, 538, 559
- Noordermeer, E., Verheijen, M. A. W. 2007, *MNRAS*, 381, 1463
- Paturel G., Petit C., Prugniel P., Theureau G., Rousseau J., Brouty M., Dubois P., Cambr  sy L., 2003, *A&A*, 412, 45
- Pfenniger, D., Revaz, Y. 2005, *A&A*, 431, 511
- Pfenniger, D., Combes, F., Martinet, L. 1994, *A&A*, 285, 79
- Persic, M. Salucci, P., Stel, F. 1996, *MNRAS*, 281, 27
- Pierce, M. J. & Tully, R. B. 1988, *ApJ*, 330, 579
- Piontek, F., Steinmetz, M. 2009, arXiv0909.4167
- Portinari, L., Sommer-Larsen, J. 2007, *MNRAS*, 375, 913
- Portinari, L., Sommer-Larsen, J., & Tantalo, R. 2004, *MNRAS*, 347, 691
- Press, W. H., Teukolsky, S. A., Vetterling, W. T., & Flannery, B. P. 1992, *Numerical Recipes in Fortran 77: The Art of Scientific Computing* (2nd ed.; Cambridge: Cambridge Univ. Press), 660
- Puech, M., Flores, H., Hammer, F., Yang, Y., Neichel, B., Lehnert, M., Chemin, L., Nesvadba, N., Epinat, B., Amram, P., Balkowski, C., Cesarsky, C., Dannerbauer, H., di Serego Alighieri, S., Fuentes-Carrera, I., Guiderdoni, B., Kembhavi, A., Liang, Y. C., Ostlin, G., Pozzetti, L., Ravikumar, C. D., Rawat, A., Vergani, D., Vernet, J., Wozniak, H. 2008, *A&A*, 484, 173
- Riffel, R., Pastoriza, M. G., Rodr  guez-Ardila, A., Bonatto, C. 2009, *MNRAS*, 400, 273
- Sanders, R. H., & McGaugh, S. S. 2002, *ARA&A*, 40, 263
- Schlegel, D.J., Finkbeiner, D.P., & Davis, M. 1998, *ApJ* 500, 525
- Spano, M., Marcelin, M., Amram, P., Carignan, C., Epinat, B., Hernandez, O. 2008, *MNRAS*, 383, 297
- Stark, D. V., McGaugh, S. S., Swaters, R. A. 2009, *AJ*, 138, 392
- Steinmetz, M., Navarro, J. F. 1999, *ApJ*, 513, 555
- Skrutskie, M. F., Cutri, R. M., Stiening, R., Weinberg, M. D., Schneider, S., Carpenter, J. M., Beichman, C., Capps, R., Chester, T., Elias, J., Huchra, J., Liebert, J., Lonsdale, C., Monet, D. G., Price, S., Seitzer, P., Jarrett, T., Kirkpatrick, J. D., Gizis, J. E., Howard, E., Evans, T., Fowler, J., Fullmer, L., Hurt, R., Light, R., Kopan, E. L., Marsh, K. A., McCallon, H. L., Tam, R., Van Dyk, S., Wheelock, S. 2006, *AJ*, 131, 1163
- Tinsley, B. M. 1981, *MNRAS*, 194, 63
- Trachternach, C., de Blok, W. J. G., McGaugh, S. S., van der Hulst, J. M., Dettmar, R. -J. 2009, *A&A*, 505, 577
- Tully, R. B. & Fisher, J. R. 1977, *A&A*, 54, 661
- Tully, R. B. & Pierce, M. J. 2000, *ApJ*, 533, 744
- van den Bosch, F. C. 2000, *ApJ*, 530, 177
- Verheijen, M. A. W. 2001, *ApJ*, 563, 694
- Williams, M. J., Bureau, M., Cappellari, M. 2009, *MNRAS*, 400, 1665
- White, S. D. M., Rees, M. J. 1978, *MNRAS*, 183, 341
- Young, J. S., Knezek, P. M. 1989, *ApJ*, 347, L55
- Zavala, J., Avila-Reese, V., Hern  ndez-Toledo, H., Firmani, C. 2003, *A&A*, 412, 633

APPENDIX A: TABLES

Table A1. NIR photometry and rotational velocities of the sample

Galaxy UGC (1)	M _H mag (2)	M _K mag (3)	V _{max} ^{RC} km s ⁻¹ (4)	V _{R(25)} ^{model} km s ⁻¹ (5)	V _{max} ^{TF} km s ⁻¹ (6)	Flags (7)
89	-24.90	-25.20	343±117	340	343±117	F-
94	-23.16	-23.40	209±21	210	209±21	F
763	-20.54	-20.74	104±11	95	104±11	F+
1256	-20.30	-20.43	105±9	119	105±9	R+
1317	-24.44	-24.69	205±9	208	205±9	F
1437	-24.42	-24.73	218±15	210	218±15	D+
1886	-24.29	-24.53	267±8	257	267±8	F+
2141	-20.98	-21.11	157±20	120	157±20	R+
2183	-22.00	-22.26	160±32	164	164±25*	F-
2503	-24.43	-24.66	285±12	291	285±12	F
2800	-20.25	-20.45	103±20	108	108±13*	R-
2855	-24.06	-24.24	229±9	221	229±9	F+
3273	-19.07	-19.25	106±7	81	106±7	R+
3334	-25.61	-25.89	377±85	385	385±62*	F-
3429	-23.89	-24.23	322±30	274	322±30	R-
3521	-22.48	-22.74	166±12	169	169±8*	F-
3528	-23.53	-23.79	276±66	273	276±66	F-
3685	-22.17	-22.40	133±177	105	133±177	R+
3691	-21.47	-21.52	143±10	131	143±10	R+
3709	-24.33	-24.65	241±14	240	241±14	F
3734	-21.36	-21.59	108±16	94	108±16	R+
3740	-21.64	-21.97	87 ±20	83	87±20	R+
3915	-23.31	-23.60	205±16	212	212±12*	F-
4026	-24.10	-24.34	284±14	282	284±14	F-
4273	-22.98	-23.22	219±11	191	219±11	R+
4284	-19.19	-19.33	118±14	103	118±14	R+
4325	-16.51	-16.70	85±13	88	88±7*	R-
4820	-23.76	-24.10	336±20	339	339±21*	F-
5175	-23.24	-23.43	188±10	199	199±6*	R-
5251	-21.74	-21.92	125±9	123	125±9	F-
5316	-19.88	-20.05	145±9	108	145±9	R+
5351	-22.35	-22.58	135±8	...	135±8	...
5721	-17.87	-18.02	99 ±29	74	99±29	R+
5789	-19.82	-20.03	131±10	92	131±10	R+
5842	-21.12	-21.35	115±18	108	115±18	R
5931	-21.46	-21.65	157±32	126	157±32	R+
5982	-22.45	-22.66	199±13	184	199±13	F-
6118	-22.93	-23.22	137±24	133	137±24	R-
6521	-23.95	-24.18	249±18	252	252±15*	F-
6537	-22.63	-22.79	187±17	197	187±17	D
6628	-17.86	-18.09	183±168	151	183±168	R+
6702	-23.54	-23.91	195±23	187	195±23	F+
6778	-22.80	-23.00	223±14	187	223±14	R+
7045	-21.98	-22.19	160±9	156	160±9	R+
7831	-20.61	-20.77	92±15	98	98±10*	R-
7861	-20.21	-20.44	50±21	33	50±21	R
7901	-23.31	-23.53	215±10	218	215±10	F
8403	-20.90	-21.07	128±10	118	128±10	R+
8490	-18.09	-18.28	90±29	89	90±29	R-
8852	-23.06	-23.28	186±10	195	195±7*	F-
8900	-24.60	-24.87	345±37	361	361±31*	R-
9179	-18.60	-18.70	111±36	105	111±36	F+
9248	-22.80	-23.05	166±11	179	166±11	F
9366	-24.74	-24.98	241±9	238	241±9	F-
9576	-21.00	-21.15	104±25	91	104±25	F+
9736	-22.64	-22.90	192±16	187	192±16	R-
9753	-21.50	-21.69	138±9	146	146±1*	F-
9866	-19.84	-20.02	114±11	115	115±7*	R-

Table A2. ...continued

Galaxy UGC (1)	M _H mag (2)	M _K mag (3)	V _{max} ^{RC} km s ⁻¹ (4)	V _{R(25)} ^{model} km s ⁻¹ (5)	V _{max} ^{TF} km s ⁻¹ (6)	Flags (7)
9969	-24.32	-24.52	311±9	321	311±9	2F
10075	-22.03	-22.25	168±9	170	168±9	1F-
10445	-17.97	-18.08	77 ±17	83	77±17	1D+
10470	-22.69	-22.92	164±39	160	164±39	1F+
10502	-23.21	-23.42	163±14	157	163±14	2F+
10521	-21.88	-22.08	124±9	128	128±4*	1R-
10546	-19.55	-19.72	106±22	106	106±22	2F+
10564	-18.10	-18.17	75 ±8	51	75±8	2R+
10757	-18.78	-19.07	81 ±33	80	81±33	2R
10897	-21.62	-21.84	113±56	117	117±35*	1R-
11012	-21.20	-21.37	117±9	127	127±1*	1F-
11218	-23.37	-23.60	185±9	188	188±4*	1F-
11269	-23.10	-23.41	202±13	197	202±13	3F+
11283	-19.50	-19.52	173±73	160	173±73	2R
11300	-19.32	-19.41	112±9	93	112±9	1R
11429	-24.73	-25.00	232±35	208	232±35	3R+
11498	-24.36	-24.62	274±9	280	274±9	3F+
11852	-23.56	-23.86	221±27	247	247±21*	3R-
11861	-22.36	-22.51	181±39	134	181±39	1R+
11872	-22.91	-23.13	183±12	188	188±8*	1F-
11914	-23.80	-24.03	285±26	283	283±27*	2D-
11951	-21.09	-21.29	106±7	102	106±7	1R+
12276	-23.55	-23.78	94 ±37	93	94±37	2F+
12343	-23.74	-23.96	221±14	243	221±14	2F+
12754	-19.64	-19.89	123±11	122	123±11	1F+

Column (1): Galaxy name. Column (2): H-band absolute magnitude. Column (3): K-band absolute magnitude. Column (4): Observed maximum rotational velocity. Column (5): Rotational velocity at R₂₅ derived from the arctan model. In the case of UGC 5351, the maximum velocity was obtained from the position velocity diagram, therefore, no arctan model could be fitted for this object. Column (6): Rotational velocities used in the TF relation. An asterisk marks the rotational velocities derived from the arctan model. In these cases, the uncertainties were computed from the kinematical inclination given in Epinat et al. (2008b). Column (7): Flag on the rotation curve (as described in the §2.1.)

Table A3. Main parameters of the GHASP sample

Galaxy UGC (1)	Radius Kpc (2)	B-V mag (3)	$\Upsilon_K^{B\&J}$ (4)	Υ_K^{BE} (5)	Υ_K^{PO} (6)	$\log M_{\star}^{B\&J}$ M_{\odot} (7)	$\log M_{\star}^{BE}$ M_{\odot} (8)	$\log M_{\star}^{PO}$ M_{\odot} (9)	$\log M_{gas}$ M_{\odot} (10)	$\log M_{bar}$ M_{\odot} (11)
89	23.30	0.85	0.73	0.81	1.18	11.31±0.10	11.35±0.10	11.52±0.10	9.92±0.05	11.37±0.10
94	...	0.78	0.66	0.79	1.04	10.54±0.10	10.62±0.10	10.74±0.10	10.03±0.05	10.72±0.08
763	...	0.77	0.65	0.79	1.03	9.47±0.10	9.56±0.10	9.67±0.10	9.45±0.04	9.81±0.06
1317	26.80	1.00	0.91	0.85	1.50	11.20±0.10	11.17±0.10	11.42±0.10	10.35±0.04	11.23±0.09
2141	4.65	0.68	0.56	0.77	0.87	9.56±0.10	9.69±0.10	9.75±0.10	9.24±0.04	9.82±0.08
2183	5.89	0.99	0.90	0.85	1.47	10.22±0.10	10.20±0.10	10.44±0.10	9.56±0.10	10.29±0.08
3521	15.65	0.77	0.64	0.79	1.01	10.27±0.11	10.36±0.11	10.47±0.11	9.97±0.05	10.51±0.08
4026	21.78	0.97	0.87	0.84	1.43	11.04±0.10	11.03±0.10	11.26±0.10	9.49±0.17	11.04±0.10
4273	15.99	0.95	0.85	0.84	1.39	10.58±0.10	10.57±0.10	10.79±0.10	9.90±0.14	10.66±0.09
4284	4.87	0.77	0.65	0.79	1.03	8.91±0.10	8.99±0.10	9.11±0.10	9.46±0.03	9.59±0.03
4325	3.80	0.87	0.75	0.82	1.21	7.92±0.12	7.96±0.12	8.13±0.12	8.91±0.03	8.96±0.03
4820	10.64	0.92	0.81	0.83	1.31	10.91±0.10	10.92±0.10	11.12±0.10	8.65±0.09	10.92±0.10
5351	8.79	0.92	0.81	0.83	1.31	10.30±0.10	10.31±0.10	10.51±0.10	8.80±0.06	10.33±0.10
5721	...	0.63	0.52	0.76	0.81	8.29±0.10	8.45±0.10	8.48±0.10	8.73±0.06	8.91±0.05
5789	...	0.64	0.53	0.76	0.82	9.10±0.10	9.26±0.10	9.29±0.10	9.56±0.03	9.74±0.04
5842	8.30	0.88	0.76	0.82	1.23	9.79±0.10	9.82±0.10	9.99±0.10	9.03±0.05	9.88±0.09
5982	11.75	0.93	0.82	0.83	1.33	10.34±0.10	10.35±0.10	10.55±0.10	9.72±0.06	10.44±0.08
6118	7.33	0.79	0.67	0.80	1.06	10.48±0.10	10.55±0.10	10.68±0.10	8.79±0.08	10.56±0.10
6521	27.69	0.84	0.71	0.81	1.14	10.89±0.10	10.94±0.10	11.09±0.10	10.15±0.04	11.01±0.09
6628	4.42	0.69	0.58	0.77	0.90	8.36±0.11	8.49±0.11	8.55±0.11	9.14±0.04	9.23±0.04
6702	21.07	0.81	0.69	0.80	1.09	10.76±0.10	10.83±0.10	10.97±0.10	9.91±0.06	10.88±0.09
6778	8.09	0.84	0.71	0.81	1.14	10.42±0.10	10.47±0.10	10.62±0.10	9.62±0.04	10.53±0.09
7045	3.48	1.66	2.45	1.04	4.54	10.63±0.10	10.26±0.10	10.90±0.10	8.93±0.04	10.28±0.10
7831	1.26	0.66	0.55	0.76	0.85	9.41±0.10	9.55±0.10	9.60±0.10	8.53±0.04	9.59±0.09
7861	2.90	0.71	0.59	0.78	0.93	9.31±0.10	9.43±0.10	9.51±0.10	8.86±0.05	9.53±0.08
7901	12.77	0.86	0.74	0.81	1.20	10.65±0.10	10.69±0.10	10.85±0.10	9.82±0.04	10.74±0.09
8403	...	0.82	0.70	0.80	1.11	9.63±0.10	9.70±0.10	9.84±0.10	9.61±0.04	9.95±0.06
8852	7.83	0.94	0.84	0.83	1.37	10.60±0.10	10.60±0.10	10.81±0.10	8.68±0.04	10.60±0.10
8900	31.39	0.99	0.90	0.85	1.47	11.26±0.10	11.24±0.10	11.48±0.10	10.33±0.08	11.29±0.09
9179	3.17	0.63	0.52	0.76	0.81	8.56±0.10	8.72±0.10	8.75±0.10	8.96±0.04	9.16±0.05
9248	16.46	0.78	0.66	0.79	1.04	10.40±0.10	10.48±0.10	10.60±0.10	9.68±0.04	10.55±0.09
9366	29.88	0.97	0.87	0.84	1.43	11.30±0.10	11.28±0.10	11.51±0.10	10.08±0.04	11.31±0.10
9576	12.05	0.67	0.55	0.77	0.86	9.57±0.11	9.71±0.11	9.76±0.11	9.83±0.06	10.07±0.06
9736	11.08	0.89	0.77	0.82	1.25	10.41±0.10	10.44±0.10	10.62±0.10	9.67±0.07	10.51±0.09
9753	9.06	0.87	0.75	0.82	1.21	9.92±0.10	9.95±0.10	10.12±0.10	9.09±0.04	10.01±0.09
9866	3.57	0.80	0.68	0.80	1.08	9.20±0.10	9.27±0.10	9.40±0.10	7.93±0.04	9.29±0.10
9969	...	0.97	0.87	0.84	1.43	11.11±0.10	11.10±0.10	11.33±0.10	10.04±0.06	11.13±0.09
10075	10.23	0.89	0.77	0.82	1.25	10.15±0.10	10.18±0.10	10.36±0.10	9.63±0.03	10.29±0.08
10445	4.31	0.68	0.56	0.77	0.87	8.35±0.11	8.48±0.11	8.54±0.11	9.28±0.04	9.35±0.03
10757	4.59	0.61	0.51	0.75	0.79	8.70±0.11	8.87±0.11	8.89±0.11	9.11±0.04	9.31±0.05

Column (1): Galaxy identification. Column (2): Optical radius taken from *SDSS*. This radius corresponds to the semimajor axis of the isophote of 25 mag arcsec⁻² (See §2.2). Column (3): Colors B-V (transformed from *SDSS* g-r colors). Columns (4), (5) and (6) list the mass-to-light ratios calculated from B&J, BE and PO, respectively. In columns (7), (8) and (9) we list the stellar masses derived from B&J, BE and PO, respectively. Column (10) lists the HI masses, corrected by helium and metals. Column (11) correspond to the baryonic mass ($M_{\star}+M_{gas}$) where M_{\star} was calculated using BE.